

Projected rainfall erosivity changes under climate change from multimodel and multiscenario projections in Northeast China

Y.-G. Zhang^{a,b}, M.A. Nearing^{b,*}, X.-C. Zhang^c, Y. Xie^a, H. Wei^b

^a School of Geography, Beijing Normal University, Beijing 100875, PR China

^b USDA-ARS, Southwest Watershed Research Center, 2000 E. Allen Rd., Tucson, AZ 85719, United States

^c USDA-ARS, Grazinglands Research Lab., 7207 W. Cheyenne St., El Reno, OK 73036, United States

ARTICLE INFO

Article history:

Received 5 May 2009

Received in revised form 17 September 2009

Accepted 17 January 2010

Accepted 17 January 2010

This manuscript was handled by K. Georgakakos, Editor-in-Chief, with the assistance of Ana P. Barros, Associate Editor

Keywords:

Climate change

Rainfall erosivity

GCM

CLIGEN

Soil erosion

Universal Soil Loss Equation

SUMMARY

Future changes in precipitation will induce changes in the erosive power of rainfall and hence changes in soil erosion rates. In this study we calculated downscaled mean annual precipitation and USLE rainfall erosivity (R) for time periods 2030 through 2059 and 2070 through 2099 in Northeast China using future precipitation predicted from six GCM models under three emissions scenarios. To accomplish this we created a new approach wherein we combined the well evaluated methods developed by Zhang (2005, 2007) for downscaling monthly precipitation products at time scales meaningful for modeling erosion processes, and the validated method developed by Yu (2002, 2003) for using a weather generator (CLIGEN) to generate accurate RUSLE erosivity factors. Changes were compared to 1960 through 1999 conditions. A stochastic weather generator (CLIGEN) calibrated to precipitation for the period 1960 through 1999 was used to temporally downscale the GCM output, from which the future R values were calculated. Our results suggested a general increase in erosivity over the region by the mid-21st century. Changes in rainfall erosivity under the higher greenhouse gas emissions scenarios, A1B and A2, exhibited the greatest projected changes. The results also indicated that changes in total annual rainfall amounts were not uniformly correspondent spatially to changes in erosivity. Multimodel means showed a generally larger increase in the northern portion of the region than that in the southern part. Future rainfall erosivity changes will have important impacts on soil and water resources in Northeastern China.

Published by Elsevier B.V.

Introduction

Global changes in temperature and precipitation patterns will impact soil erosion through multiple pathways, including precipitation and rainfall erosivity changes. In 2007, the Intergovernmental Panel on Climate Change (IPCC) concluded that human influence has contributed to the trend toward more extreme precipitation events, and that future increases in extreme precipitation are very likely (IPCC, 2007). These findings are consistent with previous studies of extreme precipitation patterns in the last century across the globe. Groisman et al. (2005) analyzed the precipitation records for over half of the land area of the globe, and found that intense precipitation frequency has increased for many extratropical regions, including China. Using a recently developed comprehensive daily precipitation dataset of China, Zhai et al. (2005) found that although there was little discernable trend in total precipitation for China as a whole, there were distinctive regional and seasonal patterns of trends, and precipitation intensity has significantly increased.

Climate change is expected to affect soil erosion based on a variety of factors, including precipitation amounts and intensities, temperature impacts on soil moisture and plant growth, and direct fertilization effects on plants due to greater CO₂ concentrations, among others. The most direct impact results from the change in the erosive power of rainfall (Nearing, 2001). Rainfall erosivity represents a measure of erosive force of rainfall to cause soil erosion. The rainfall erosivity for a given storm, as most commonly calculated for use in the Universal Soil Loss Equation (USLE) (Wischmeier and Smith, 1978) or its revision, RUSLE (Revised USLE) (Renard et al., 1997), is equal to the product of total storm energy (E) and maximum 30-min rainfall intensity (I_{30}), or EI_{30} . The R -factor is defined as the average annual sum of EI_{30} calculated from a rainfall record.

Current GCMs do not provide detailed precipitation information that enables the calculation of the R -factor directly as a function of rainfall intensity and energy. Therefore, statistical relationships between monthly and annual precipitation and rainfall erosivity have been used to study the R -factor changes with GCM outputs (Nearing, 2001; Renard and Freidmund, 1994). Nearing (2001) used these methods to estimate potential changes in R -factor from two GCMs outputs across the contiguous United States in the 21st century. Nearing (2001) estimated that the average of

* Corresponding author. Tel.: +1 520 670 46481x152.

E-mail address: mark.nearing@ars.usda.gov (M.A. Nearing).

magnitude of change across the country ranged between 16% and 58%, with some areas showing increases and other areas showing decreases. With a similar method, Zhang et al. (2005) projected potential changes in rainfall erosivity from HadCM3 in the Huanghe River Basin of China, and concluded that the rainfall erosivity would increase by as much as 11–22% by the middle of the 21st century across the region. However, these relationships have limitations, particularly with regard to snow dominated areas, and do not consider the impact of large changes in the storm intensity or duration on rainfall erosivity.

Stochastic weather generators are often used to generate long-term, daily weather series for modeling applications, such as with the process-based WEPP model (Flanagan and Nearing, 1995). They have also been used to generate daily climate files from monthly GCM-projections for climate change impact studies (e.g., Mearns et al., 1997; Wilks, 1999; Pruski and Nearing, 2002a; Zhang, 2005). Yu (2002, 2003) assessed the ability of the CLimate GENerator (CLIGEN) (Nicks and Gander, 1994) to generate RUSLE climate files for 165 sites in US and 43 sites in Australia and found that the generated *R*-factor was highly correlated with the measured *R*-factor, although the generated *R*-factor was systematically overestimated because of the particular storm pattern adopted in WEPP, rather than an intrinsic deficiency of CLIGEN. Thus, CLIGEN together with calibration formulas to adjust the generated *R*-factor is able to adequately generate the *R*-factor for RUSLE. This application of CLIGEN is superior to existing methods used to estimate *R*-factor from only monthly precipitation data, which is often the only information available from GCM outputs (Yu, 2002, 2003). Generating erosivity using CLIGEN facilitates consideration of the impact of rainfall intensity and duration on potential changes in rainfall erosivity and soil erosion. Moreover, Nicks and Gander (1994) also calculated the *R*-factor using CLIGEN for the eastern US, and found that the isoerodent map was quite similar to those given in the USLE handbook (Wischmeier and Smith, 1978).

There exists spatial and temporal scale mismatch between GCM-projections and point-scale impact assessment of climate change (Murphy, 1999). The spatial resolution of the GCM is often coarser than that needed for assessing local impacts of climate change on natural resources. Zhang (2005, 2007) developed an explicit method for spatial-temporal downscaling of GCM monthly precipitation projections to daily weather data series using CLIGEN. The method scales to a site-specific station explicitly considering the spatial differences between climate variability at the two scales. CLIGEN can then be used to further disaggregate monthly climate values to daily weather series at the station scale.

The objective of this study was to assess potential changes in projected future precipitation and rainfall erosivity to climate change in northeastern China for the period of 2030–2059 and 2070–2099 from multiple models and scenarios. To do this we created a new approach wherein we combined the well evaluated methods developed by Zhang (2005, 2007) for downscaling monthly precipitation products at time scales meaningful for modeling erosion processes, and the validated method developed by Yu (2002, 2003) for using a weather generator (CLIGEN) to generate accurate RUSLE erosivity factors. In addition to producing a quantification of projected rainfall erosivities for the region, we found that changes in total annual rainfall amounts were not uniformly correspondent spatially to changes in erosivity.

Materials and methods

Study area and observed data

The study area, located in the northeast of China, covers 1,240,000 km² and had a population of approximately 107 million

in 2002 (NBSC, 1998–2003). It comprises Heilongjiang, Jilin, Liaoning Provinces, and a portion of the Inner Mongolia (Fig. 1). The climate is a semi-humid continental climate with long, cold winters and short, wet summers. The annual precipitation decreases from southeast (900 mm) to northwest (400 mm), with irregular rainfall distribution; high-intensity rainstorms occur during summer, and have a high erosive potential.

The region is one of China's primary production areas of commercial food grains (maize, rice) and economic crops (soybean, sugar beets, etc.). The area has experienced significant warming over the last 100 years (Liu et al., 2004). Based on observed weather data in northeastern China over the prior 50 years, Qian and Lin (2005) found a trend toward warmer conditions over the entire region, and a trend toward wetter conditions in the northern part of the region, along with trends of increases in both precipitation intensity and frequencies of extreme precipitation events. For the southern part of the region, they found trends toward warmer and drier conditions, with a decrease in large storms and precipitation intensities and decrease in the frequency of persistent wet days (Qian and Lin, 2005). According to the IPCC AR4, an increase in precipitation was projected in this region in all seasons (IPCC, 2007). Meanwhile, intense precipitation events are very likely to increase, consistent with the historical trend in this region (Zhai et al., 2005).

Databases from the China National Meteorological Centre (CNMC) were used to extract daily precipitation and temperature data for 1960 through 1999 from 107 stations within the study area as a baseline condition for assessing the change in future climate predictions. The stations included all the first- and second-class national climate stations in northeastern China, and the climate data were compiled and quality-controlled by the CNMC. A screen check on missing precipitation and temperature data was conducted to ensure all the stations have more than 30 years climate records. 92 out of 107 stations were retained in our database. We recognize that the rainfall measurements were undoubtedly impacted by wind. In that sense, the measurements used are similar to those that were used in the original data for producing *R*-factor relationships (Wischmeier and Smith, 1978).

Climate change scenarios

To estimate the potential future climate we used data from the recent IPCC AR4 coupled ocean-atmosphere GCM simulations (IPCC, 2007). Previous studies have suggested that regional climate change projections from different GCM simulations were quite different. The results varied spatially (NRC, 2003; Giorgi and Mearns, 2002), and the differences were more significant in precipitation predictions than in temperature predictions (Vidal and Wade, 2008). Therefore, six GCMs were used to obtain the monthly precipitation and surface air temperature (Table 1). To represent the different greenhouse gas (GHG) emissions scenarios, three non-mitigated IPCC Special Report on Emissions Scenarios (SRES): A2, A1B and B1, were selected. The three scenarios (A2, A1B and B1) represent 'high', 'medium' and 'low' GHG emissions scenarios (IPCC, 2007). The three scenarios were implemented for all six models during two time slices of 30 years each, from 2030 through 2059 and from 2070 through 2099, except for scenario B1 for the HadGEM1 model, due to its absence on the IPCC-DDC website. To calibrate the GCM results, we also collected data from the 'Climate of the 20th Century' experiment (20C3M), which simulates climate conditions during 1850–2000 that was driven by the pre-industrial GHG emissions. The 20C3M run during 1960–1999 was used as the baseline period. Recent studies showed that the multimodel ensemble simulated reasonably well the summer monsoon precipitation and annual cycles for the late 20th century in the study area (Kripalani et al., 2007; Lee et al., 2008). However, the inter-model

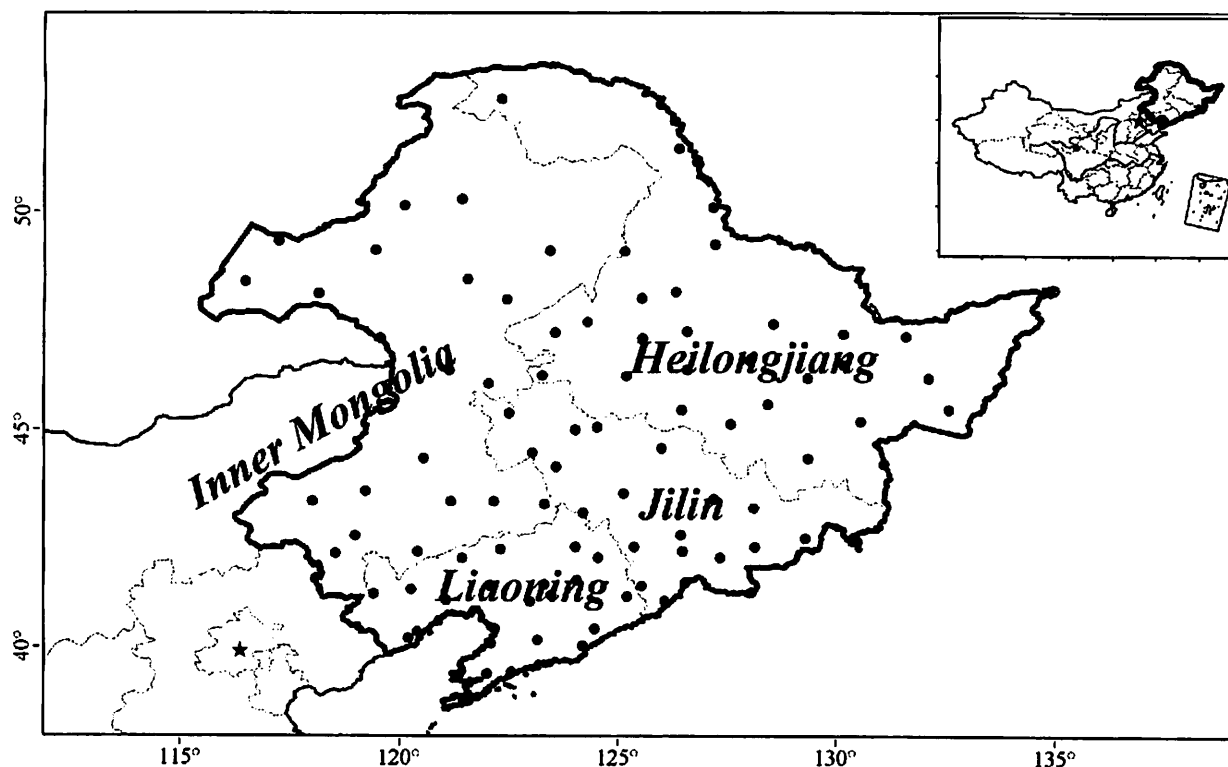


Fig. 1. Location of study area.

Table 1
Summary of General Circulation Models (GCMs) used in this study.

CGCM	Research centre	Resolution	Country
CGCM3.1 (T47)	Canadian Centre for Climate Modeling and Analysis, Canada	3.75° × 3.75°	Canada
CGCM3.1 (T63)	Canadian Centre for Climate Modeling and Analysis, Canada	2.8° × 2.8°	Canada
CSIRO-MK3.0	Commonwealth Scientific and Industrial Research Organization (CSIRO) Atmospheric Research, Australia	1.875° × 1.875°	Australia
UKMO-HadCM3	Hadley Centre for Climate Prediction and Research/Met Office, UK	2.5° × 3.75°	UK
UKMO-HadGEM1	Hadley Centre for Climate Prediction and Research/Met Office, UK	1.25° × 1.875°	UK
ECHAM5/MPI-OM	Max Planck Institute for Meteorology, Germany	1.875° × 1.875°	Germany

variability is slightly larger in summer precipitation (Kripalani et al., 2007; IPCC, 2007), implying the needs to calibrate the GCM 20C3M runs with observed data for future changes.

Downscaling and R-factor calculations

A spatio-temporal downscaling process (Zhang, 2005, 2007) was used to downscale monthly precipitation of GCM-projections at scale of GCM-grid boxes to scale of specific weather stations.

Spatial downscaling

Spatial downscaling in this study was performed between a station and a GCM-grid box containing the station following the methods of Zhang (2007). First, we produced QQ-plots of the observed monthly precipitation data for the time period of 1960–1999, ranked in order of magnitude, using the corresponding data from 20C3M. We then derived both linear and non-linear regression functions between the two sets of ranked values for each month. The use of the non-linear transfer function was taken from Zhang (2007), who found that the non-linear function produced a superior transfer function in some cases. Hence, the monthly pre-

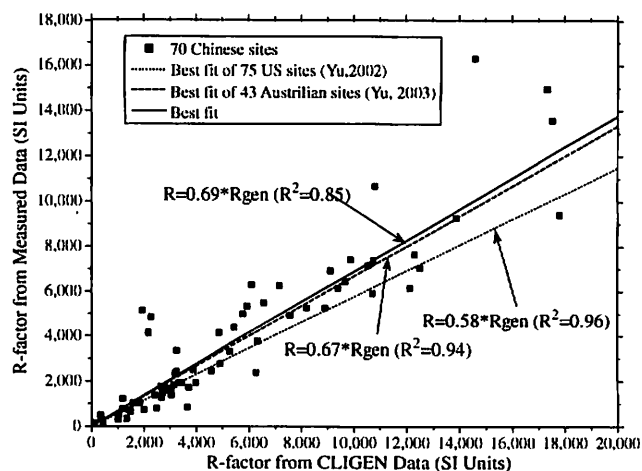


Fig. 2. Relationship between the R-factor estimated using CLIGEN and the R-factor based on measured precipitation data for 70 sites in China.

cipitation amounts of 1960–1999 from the 20C3M experiment were used as the control, and the historical monthly data of the

same period were used as the baseline climate condition. Then the regression functions were applied to the GCM-projected future precipitation of each month. The non-linear function was used for precipitation values within the range in which the function was fitted, and the linear function was used for the values outside

the range to generate conservative, first-order approximations. For each calendar month, 30-year-downscaled monthly precipitation values were obtained at each station for the two future time slices. Then the monthly means and variances of the future climate at each station were calculated.

Table 2

Mean, standard deviation, maximum, and minimum of annual precipitation calculated by Kriging based on the 92 sites across the study area, and the spatial mean percentage changes, as simulated by the six models under the three emission scenarios.

	2030–2059			2070–2099		
	A2	A1B	B1	A2	A1B	B1
<i>Observation (1960–1999)</i>						
Mean (mm)				504		
SD (mm)				125		
Max. (mm)				1042		
Min. (mm)				278		
<i>CGCM3.1 (T47)</i>						
Mean (mm)	593	605	580	709	632	605
SD (mm)	152	140	150	164	156	152
Max. (mm)	1209	1213	1233	1380	1321	1204
Min. (mm)	280	321	298	374	324	281
Mean change (%)	17.7	20.0	15.1	40.7	25.4	20.0
<i>CGCM3.1 (T63)</i>						
Mean (mm)	609	627	603	703	652	627
SD (mm)	155	156	133	143	155	129
Max. (mm)	1345	1260	1124	1256	1322	1118
Min. (mm)	311	320	322	419	333	337
Mean change (%)	20.8	24.4	19.6	39.5	29.4	24.4
<i>CSIRO-MK3.0</i>						
Mean (mm)	593	603	565	621	605	615
SD (mm)	144	157	122	133	146	274
Max. (mm)	1152	1214	988	1105	1133	1260
Min. (mm)	310	306	285	325	285	293
Mean change (%)	17.7	19.6	12.1	23.2	20.0	22.0
<i>UKMO-HadCM3</i>						
Mean (mm)	564	585	545	688	682	592
SD (mm)	140	139	128	197	151	167
Max. (mm)	1112	1092	988	1659	1229	1396
Min. (mm)	294	313	293	252	356	287
Mean change (%)	11.9	16.1	8.1	36.5	35.3	17.5
<i>UKMO-HadGEM1</i>						
Mean (mm)	534	530	/	551	546	/
SD (mm)	99	121	/	113	114	/
Max. (mm)	927	1066	/	1070	1166	/
Min. (mm)	308	290	/	313	303	/
Mean change (%)	6.0	5.2	/	9.3	8	/
<i>ECHAM5/MPI-OM</i>						
Mean (mm)	490	533	559	551	536	524
SD (mm)	121	111	112	125	121	131
Max. (mm)	1042	891	955	1047	884	1048
Min. (mm)	252	301	307	311	283	255
Mean change (%)	-2.8	5.8	10.9	9.3	6.3	4.0

Table 3

Averages and sample standard deviations across the six GCMs of spatially averaged, annual precipitation and rainfall erosivity (R) values, their changes relative to 1960–1999 observed data and ratios of average changes in annual precipitation to average changes in annual erosivity.

	Observation (1960–1999)	2030–2059			2070–2099			
		A2	A1B	B1	A2	A1B	B1	
Annual precip.	Mean (mm)	504	564	581	570	637	609	593
	(P)		(0.018)	(0.005)	(0.003)	(0.007)	(0.008)	(0.008)
	St. dev. (mm)		45	40	22	73	58	40
	% Change		12	15	13	26	21	18
Annual erosivity	Mean (MJ mm h ⁻¹ ha ⁻¹)	1776	2642	2619	2660	3397	3037	2822
	(P)		(0.002)	(0.001)	(0.001)	(0.000)	(0.000)	(0.002)
	St. dev. (MJ mm h ⁻¹ ha ⁻¹)		381	337	233	312	253	334
	% Change		49	64	50	91	71	59
Ratio of % change of erosivity to precip.			4.1	4.2	3.8	3.4	3.4	3.4

Temporal downscaling

Temporal downscaling was done in order to estimate CLIGEN input parameters used to generate daily weather series representing the future climates. The baseline CLIGEN input parameters were determined by measured daily weather data of 1960–1999

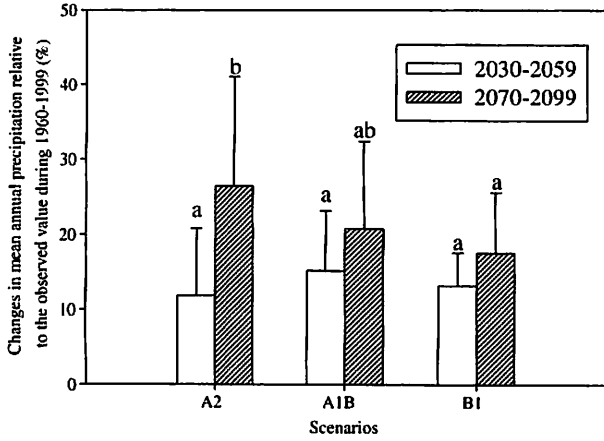


Fig. 3. Changes in mean annual precipitation during 2030–2059 and 2070–2099 relative to 1960–1999 under three emission scenarios. Each value is the mean of six models averaged over the region (\pm SD). Different letters indicate significant differences at $P < 0.05$ (Duncan's test).

at each station. Four precipitation parameters were required adjustment for running CLIGEN to generate future daily weather series: R_d , daily mean precipitation; σ_d^2 , the variance of daily precipitation for wet days (days with non-zero precipitation); $P_{w/d}$, conditional transition probabilities of a wet day following a dry day; and $P_{w/w}$, conditional transition probabilities of a wet day following a wet day.

To determine $P_{w/w}$ and $P_{w/d}$, we separated the 40 years of observed data into two groups with 20 wettest and driest months in each group, based on the rank of daily precipitation values and calculated the $P_{w/w}$ and $P_{w/d}$ for each group (Zhang, 2007). A linear relationship between $P_{w/w}$ and mean monthly precipitation (R_m), as well as relationship between $P_{w/d}$ and R_m were developed based on two pairs of data points. Future conditional transition probabilities of precipitation were estimated from this linear relationship. For convenience, two parameters are often defined for the Markov chain:

$$\pi = \frac{P_{w/d}}{1 + P_{w/d} - P_{w/w}} \quad (1)$$

$$r = P_{w/w} - P_{w/d} \quad (2)$$

representing the unconditional probability of daily precipitation occurrence (π) and the lag-1 autocorrelation of daily precipitation series (r).

The adjusted mean daily precipitation per wet day (R_d) was estimated as:

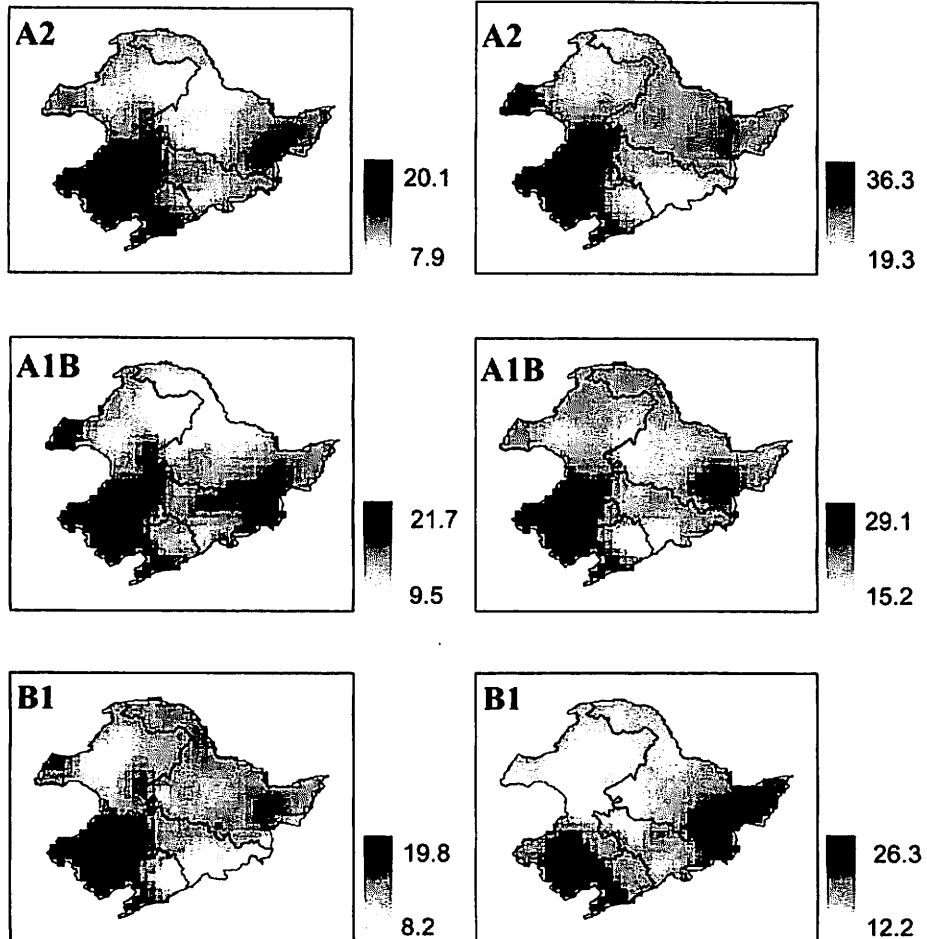


Fig. 4. Spatial variation of changes (%) in mean annual precipitation as simulated by six models for 2030–2059 (left) and 2070–2099 (right) relative to 1960–1999 under three scenarios across the study area.

$$R_d = \frac{R_m}{N_d \pi} \quad (3)$$

N_d is the number of days in the month and $N_d \pi$ is the average number of wet days in the month. New daily precipitation variance (σ_d^2) related to monthly precipitation variance at the station was obtained in (Wilks, 1999):

$$\sigma_d^2 = \frac{\sigma_m^2}{N_d \pi} - \frac{(1 - \pi)(1 + r)}{1 - r} R_d^2 \quad (4)$$

Computation of daily precipitation variance was problematic for winter months, and in some cases negative daily precipitation variance values were generated from Eq. (4) for some winter months on some sites. This was found also by Zhang et al. (2004), who attributed the problem to the relatively small variance of projected monthly precipitation for the future winter periods compared with measured monthly precipitation. For those months, a simple proportional adjustment method (Zhang et al., 2004) was

used by multiplying the baseline variance (derived from daily station records) by the variance ratio of projected monthly precipitation between 1960–1999 and 2030–2059 (or 2070–2099) period. However, this scaling method had negligible effect on the R -factor calculation because rainfall amounts were relatively small during winter months in the study area.

Finally, all parameters at each station were adjusted separately for each climate change scenario. These adjusted parameters were then input to CLIGEN (V5.22564), and 100 years of daily series data were generated for each station under each climate change scenario and each GCM.

Algorithm of R-factor calculation

The outputs of 100 years of daily series at each station from CLIGEN were used to extract precipitation amounts, P (mm), storm duration, D (h), time to peak as a fraction of storm duration, t_p , and the ratio of peak intensity over the average intensity, i_p , in order to calculate R -factors (Nicks et al., 1995). The algorithm and steps were described in detail by Yu (2002, 2003), and briefly summarized as follows.

Storms on wet days that have mean air temperature greater than 0° were selected. The peak 30 min rainfall intensity (I_{30}) for each storm was calculated using Eqs. (5) (for storms with $D < 30$ min) and (6) (for storms with $D > 30$ min):

$$I_{30} = 2P \quad (5)$$

$$I_{30} = \frac{2P i_p}{b t_p} \left(1 - e^{-\frac{b t_p}{I_p}} \right) \quad (6)$$

where b is parameter for the storm pattern.

The storm energy (E) for each chosen storm was calculated as the integration of unit energy (e) over the double exponential storm pattern in CLIGEN:

$$E = P e_0 \left[1 - \frac{\alpha i_p}{b t_p} \frac{I_0}{I_p} \left(e^{-\frac{I_0}{b t_p}} - e^{-\frac{I_0}{b t_p}} \right) \right] \quad (7)$$

where I_p is peak intensity (mm h^{-1}) and e is the unit energy calculated using the erosivity equation in RUSLE (Renard et al., 1997):

$$e(i) = e_0 (1 - \alpha e^{-i/I_0}) \quad (8)$$

where $e_0 = 0.29 \text{ MJ ha}^{-1} \text{ mm}^{-1}$, $\alpha = 0.72$, and $I_0 = 20 \text{ mm h}^{-1}$ (Brown and Foster, 1987).

Rainfall erosivity (EI), defined as the product of I_{30} and E , was calculated for each storm and then the monthly mean EI were

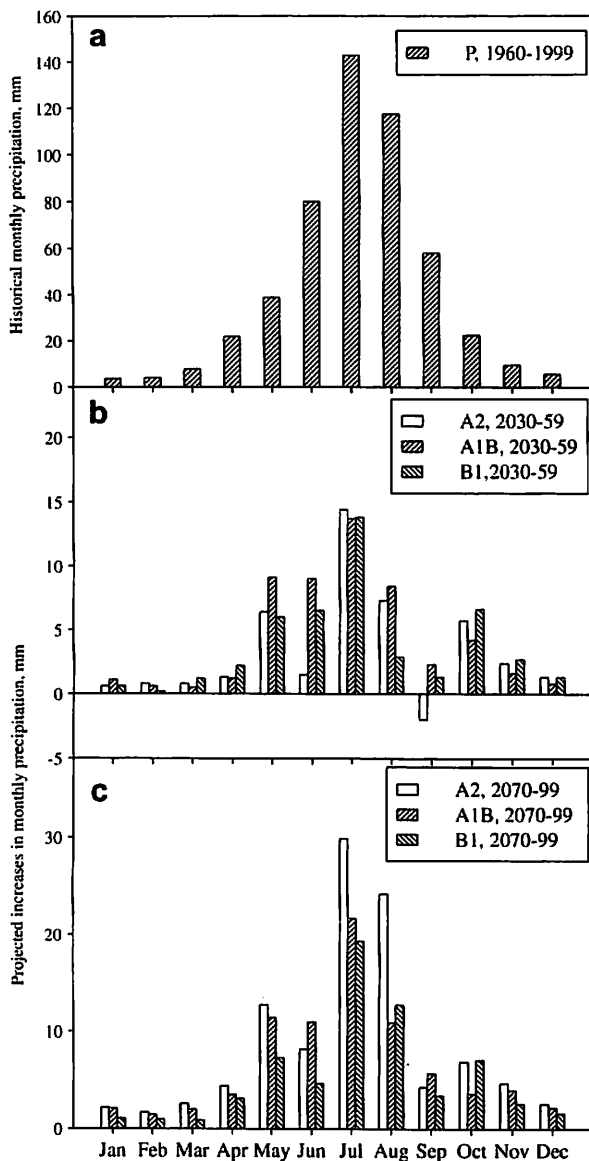


Fig. 5. (a) Spatially-averaged, measured monthly precipitation for 1960–1999; (b) projected area-averaged differences in monthly precipitation during 2030–2059 relative to 1960–1999 over the region; and (c) during 2070–2099 relative to 1960–1999 over the region. Each projected value is the mean of six models averaged over the region.

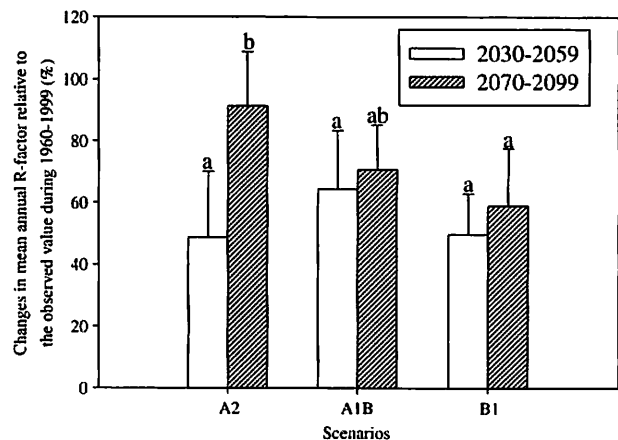


Fig. 6. Relative changes in R -factor during 2030–2059 and 2070–2099 relative to 1960–1999 ($1776 \text{ MJ mm h}^{-1} \text{ ha}^{-1}$) under three scenarios. Each value is the mean of six models averaged over the region ($\pm \text{SD}$). Different letters indicate significant differences at $P \leq 0.05$ (Duncan's test).

obtained to compute the *R*-factor, which is the sum of monthly mean EI. A program called CLG2RF (Yu, 2002) was modified in this study to implement the algorithm described above.

In order to assess CLIGEN's ability to estimate the *R*-factor, daily weather data and measured *R*-factor (*R*) during 1951–2007 for 70 sites in China were collected. Daily precipitation and temperature data from the 70 sites were then input to CLIGEN, and 100 years of climate data for each site were generated. Then CLG2RF were used to estimate the mean annual rainfall erosivity (R_{gen}) for each of the 70 sites. A calibration relationship was derived between R_{gen} and *R* in a similar way as was done for the US and Australia (Yu, 2002, 2003) (Fig. 2). This relationship then allowed us to estimate *R*-factors for the future climate scenarios.

Computer programs were written to implement the *R*-factor algorithm at all 92 sites under three scenarios for six GCM models. After the precipitation and *R*-factor values were obtained, the results were then interpolated onto a common grid ($0.5^\circ \times 0.5^\circ$) with Kriging method for spatial averaging and comparison purposes. Statistical analysis was performed using the SAS program (SAS Instituted Inc., 2003). A *t*-test and Duncan's multiple range test were used to determine significant differences in mean precipitation and rainfall erosivity changes among the models, scenarios and periods.

Results and discussion

Projected precipitation changes

Table 2 presents individual model-projected mean annual precipitation and its changes averaged over the region during the two future periods under the three scenarios. The models projected increases over the region with the exception of the model ECHAM5 during the period of 2030–2059 under the A2 scenario (–2.8%). Overall, the model CGCM3.1 (T63) simulated the highest increases in mean precipitation in the six models during the period of 2030–2059 and 2070–2099 under all the three scenarios, while ECHAM5 and HadGEM1 projected the least increases.

Comparison of means testing (*t*-test) showed that the future mean annual precipitation values averaged over the region and averaged from six model predictions were significantly greater ($\alpha = 0.05$) under all three scenarios for both future time slices compared to the observed mean precipitation of 504 mm during 1960–1999 (Table 3). For the period of 2030–2059, the increases in mean annual precipitation were not significantly different between the three scenarios using a Duncan means test ($\alpha = 0.05$) (Fig. 3). For the period of 2070–2099, significantly greater increases in mean precipitation were projected under the higher emissions scenario,

Table 4

Mean, standard deviation, maximum, and minimum of annual rainfall erosivity (*R*) calculated by Kriging based on the 92 sites across the study area, and the spatial mean erosivity changes, as simulated by the six models under the three emission scenarios.

	2030–2059			2070–2099		
	A2	A1B	B1	A2	A1B	B1
<i>Observation (1960–1999)</i>						
Mean (MJ mm h ⁻¹ ha ⁻¹)			1776			
SD (MJ mm h ⁻¹ ha ⁻¹)			547			
Max. (MJ mm h ⁻¹ ha ⁻¹)			3933			
Min. (MJ mm h ⁻¹ ha ⁻¹)			862			
<i>CGCM3.1 (T47)</i>						
Mean (MJ mm h ⁻¹ ha ⁻¹)	2365	2790	2506	3397	2691	2634
SD (MJ mm h ⁻¹ ha ⁻¹)	484	554	640	805	758	819
Max. (MJ mm h ⁻¹ ha ⁻¹)	4321	4381	5320	5871	4937	5538
Min. (MJ mm h ⁻¹ ha ⁻¹)	1453	1644	1279	1909	1497	1180
Mean change (%)	33.2	57.1	41.1	91.3	51.5	48.3
<i>CGCM3.1 (T63)</i>						
Mean (MJ mm h ⁻¹ ha ⁻¹)	2810	3396	2947	3675	3058	2989
SD (MJ mm h ⁻¹ ha ⁻¹)	707	886	640	769	993	544
Max. (MJ mm h ⁻¹ ha ⁻¹)	5192	6091	4485	5474	6522	4916
Min. (MJ mm h ⁻¹ ha ⁻¹)	1518	1770	1583	1910	1540	1884
Mean change (%)	58.2	91.2	65.9	106.9	72.2	68.3
<i>CSIRO-MK3.0</i>						
Mean (MJ mm h ⁻¹ ha ⁻¹)	3162	3229	2610	3260	3235	3181
SD (MJ mm h ⁻¹ ha ⁻¹)	877	1225	513	741	821	1159
Max. (MJ mm h ⁻¹ ha ⁻¹)	6477	7034	4489	5976	5976	6806
Min. (MJ mm h ⁻¹ ha ⁻¹)	1710	1263	1709	1609	1747	1439
Mean change (MJ mm h ⁻¹ ha ⁻¹)e	78.0	81.8	47.0	83.6	82.2	79.1
<i>UKMO-HadCM3</i>						
Mean (MJ mm h ⁻¹ ha ⁻¹)	2828	2855	2847	3792	3360	2968
SD (MJ mm h ⁻¹ ha ⁻¹)	983	769	761	1084	795	1066
Max. (MJ mm h ⁻¹ ha ⁻¹)	6979	5766	5818	8317	6039	7959
Min. (MJ mm h ⁻¹ ha ⁻¹)	1254	1395	1512	1775	1863	1430
Mean change (%)	59.2	60.8	60.3	113.5	89.2	67.1
<i>UKMO-HadGEM1</i>						
Mean (MJ mm h ⁻¹ ha ⁻¹)	2606	2777	/	3341	3074	/
SD (MJ mm h ⁻¹ ha ⁻¹)	683	734	/	839	806	/
Max. (MJ mm h ⁻¹ ha ⁻¹)	5328	5486	/	5867	6674	/
Min. (MJ mm h ⁻¹ ha ⁻¹)	1473	1796	/	1843	1985	/
Mean change (%)	46.7	56.4	/	88.1	73.1	/
<i>ECHAM5/MPI-OM</i>						
Mean (MJ mm h ⁻¹ ha ⁻¹)	2082	2469	2388	2915	2801	2339
SD (MJ mm h ⁻¹ ha ⁻¹)	414	479	437	932	788	620
Max. (MJ mm h ⁻¹ ha ⁻¹)	3541	3274	3304	7091	4727	4543
Min. (MJ mm h ⁻¹ ha ⁻¹)	1273	1279	1233	1502	1349	1229
Mean change (%)	17.2	39.0	34.5	64.1	57.7	31.7

A2, compared to the lowest emissions scenario, B1 ($\alpha = 0.05$). These projected increases in precipitation in the study area are comparable to other results of increases over high latitude northern hemisphere regions (up to 20% or more) (Giorgi and Bi, 2005).

Differences of projected precipitation changes across the models, as quantified by the standard deviation, were greater for the 2070–2099 period than for 2030–2059 for all three emission scenarios (Table 3). Standard deviations were also greater for the scenarios with the greater level of anthropogenic forcing levels (i.e., A2 vs. A1B vs. B1). The increase in variance between climate projections for the later time period was indicative of the fact that the GCM models cannot be expected to project as well over the longer time period or under condition of greater forcing. These results agree with those of Kharin et al. (2007), who reported that the inter-model uncertainties in extreme precipitation changes increased significantly with the increased anthropogenic forcing.

Fig. 4 shows the spatial patterns of the multimodel-averaged relative change (%) in mean annual precipitation using the observed annual mean precipitation of 504 mm during 1960–1999 as a reference value. The smallest value of the change was a positive 7.9% during 2030–2059 under the A2 scenario, which indicated that the projected mean annual precipitation increased over the entire study area during the both future time periods under all three scenarios. The general spatial trend showed the greater increases in the southwestern and eastern areas for both time periods under all scenarios, and lesser increases in the northern and central parts of the region occupying the Greater XingAn Mountains, Small XingAn Mountains, Changbai Mountain and Songnen Plain.

Fig. 5 shows results for projected monthly mean precipitation changes, averaged across the six GCM model outputs. Overall projected precipitation showed increases for every month during both future periods and under all three emission scenarios, except the September for the A2 scenario during 2030–2059. The seasonal pattern of monthly mean precipitation estimated by the three emission scenarios was similar during the two periods, with greater increases in precipitation during the summer months. The absolute changes in precipitation were also larger in most months for 2070–2099 than for 2030–2059.

Projected rainfall erosivity changes

The trends in scenario-averaged, projected annual erosivity changes followed the same basic pattern as did the trends in precipitation (Fig. 6). As with precipitation, projected erosivity values were significantly greater ($\alpha = 0.05$) than those for the period 1960–1999 in all cases. As expected, the greatest rainfall erosivity was simulated in 2070–2099 under the A2 scenario. Of the six models, the model ECHAM5 projected the smallest increases in erosivity, while the models CGCM3.1 (T63) and CSIRO-MK3.0 projected the greatest increases (Table 4).

Overall, the methods outlined here show an increase of between 17% and 91% in rainfall erosivity by mid-century, and between 32% and 114% by the end of the century (Table 3). These magnitudes of percent change were 3.4–4.2 times greater for erosivity than for precipitation. This is consistent with the previous studies from other places (Pruski and Nearing, 2002b; Nearing et al., 2005). This may be an important finding in terms of erosion forecasting for this

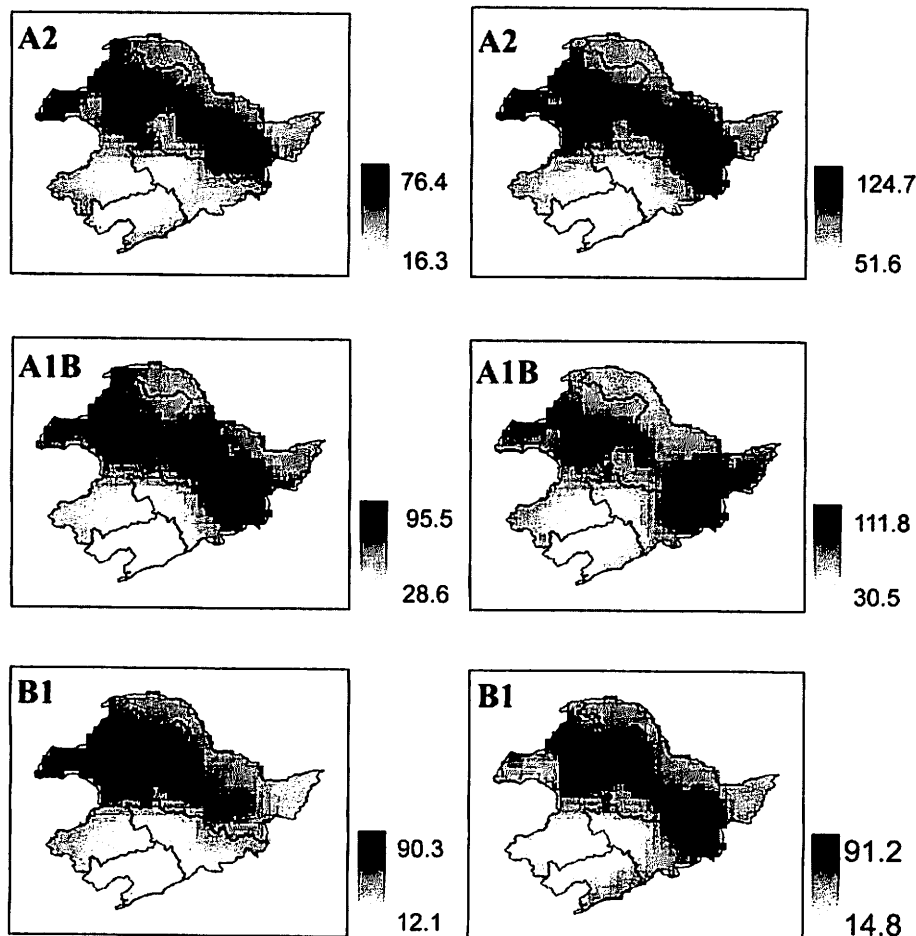


Fig. 7. Spatial variation of changes (%) in mean annual rainfall erosivity as simulated by six models during 2030–2059 (left) and 2070–2099 (right) relative to 1960–1999 under three scenarios across the study area.

area. The trends in the results suggest that erosion rates in this region could increase dramatically more than that precipitation amount changes alone might suggest.

The projected spatial patterns in erosivity changes (Fig. 7) from multimodel scenarios are depicted as differences (in percentage) between the mean downscaled GCM-projections from the six IPCC AR4 models in 2030–2059 (left) and 2070–2099 (right) relative to 1960–1999 under the three emission scenarios studied. Projected rainfall erosivity increased over the entire region. The models tended to project greater relative increases in erosivity in the northern region compared to the southern portion. These spatial patterns differ from those of projected changes in annual mean precipitation in the region (Fig. 4), indicating that there must be greater projected changes in rainfall intensity and energy for the northern region than for the south. These findings are consistent with previous studies in historical precipitation changes over the region (Qian and Lin, 2005; Zhai et al., 2005), where precipitation intensity was shown to have significantly increased in the northern

region during the last 50 years, while decreasing in the southern region.

The summer months in this region have the highest levels of rainfall erosivity, and these are also the months projected to have the greatest increases in erosivity under a changing climate (Fig. 8), indicating that increases in precipitation amounts are generally accompanied by increases in precipitation intensity. Rainfall erosivities during May through October show increases during both future periods and under all three emission scenarios, with particularly large increases during the months of July through September. This result is generally consistent with the seasonal trends of mean monthly precipitation (Fig. 5).

Summary and conclusions

In this study, we evaluated the potential changes in precipitation and rainfall erosivity in the northeastern China for three future climate scenarios A2, A1B and B1 from six GCMs using spatial-temporal downscaling techniques. The future projections of precipitation for northeast China in this study agree with the majority of the GCMs from the IPCC AR4 that show very likely precipitation increases in East Asia for both winter and summer for the 21st century (IPCC, 2007; Kripalani et al., 2007). The models predicted the greatest precipitation increases in the southwestern and eastern region. However, greater erosivity increases were projected over the northern region than over the southern region. This disparity in spatial trends between total precipitation and rainfall erosivity is due to greater projected increases in rainfall intensities and storm energies in the northern part of the study area, and is consistent with analyses of historical data (Qian and Lin, 2005; Zhai et al., 2005). Our results also suggested that rainfall erosivity would increase at a greater rate (by a factor of 3.4–4.2) than the precipitation.

The projected increases in future rainfall erosivity forewarns important trends of soil loss and runoff in the northeastern China. Based on the USLE or RUSLE estimates, a 1% increase in rainfall erosivity will cause a 1% increase in soil loss assuming other factors related to crops, management, and conservation practices remain the same. Previous studies have shown that the Northeastern China has experienced severe water erosion after about 100 years of intensive cultivation (Zhang et al., 2007; Wu et al., 2008). Unlike agricultural lands in the US or on the Loess Plateau of China, there are few vegetation and engineering conservation measures in place for soil erosion control in northeastern China. The expected increase in erosivity will impose more pressure on the land resources, and may have a significant negative impact on agricultural production. Our study highlights the need to design, plan and implement soil conservation practices to combat potentially severe soil erosion in this region under climate change.

The contribution of this work is the combined utilization of two previously published, tested, and proven methods to allow one to use GCM output to make projections regarding USLE- and RUSLE-type rainfall erosivities. This has potentially important implications for conservation planning worldwide. As we look forward to a changing future for rainfall erosivity, there is a need for more careful monitoring and updates related to erosivity, which is a critical component for conservation planning and for implementing conservation programs. This work provides a step towards facilitating conservation planning in a non-stationary climate.

Acknowledgments

This research was partially supported by the National Basic Research Program of China (2007CB407204) and the USDA Agricultural Research Service. We acknowledge the international modeling groups for providing their data for analysis, the IPCC Data

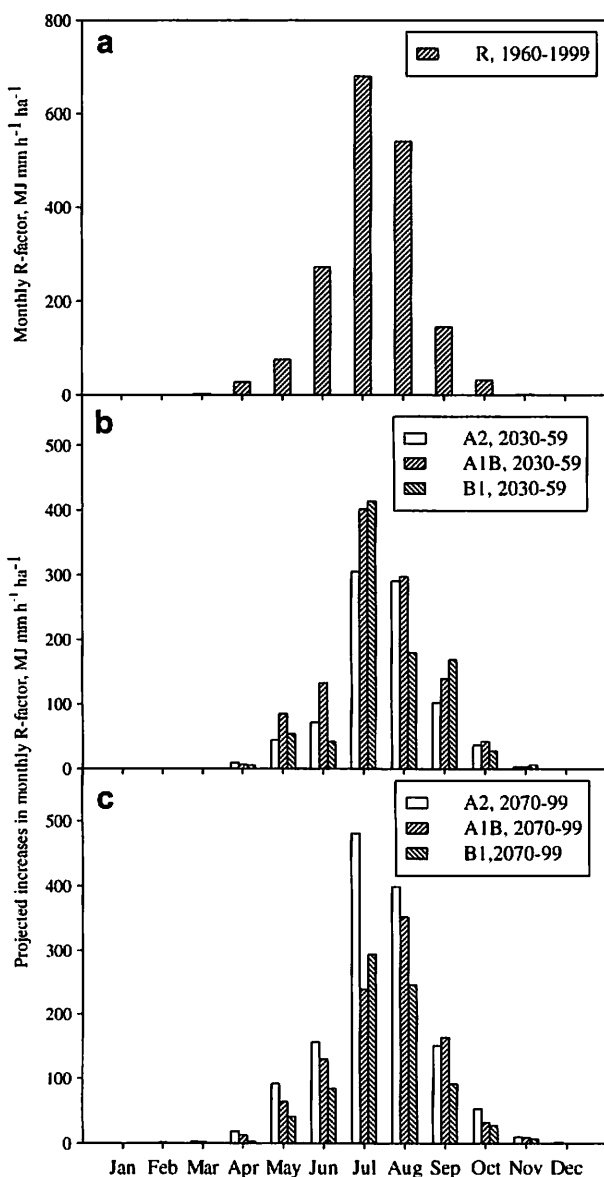


Fig. 8. (a) Spatially-averaged, measured monthly erosivities (R) for 1960–1999; (b) projected area-averaged differences in monthly erosivities during 2030–2059 relative to 1960–1999 over the region; and (c) during 2070–2099 relative to 1960–1999 over the region. Each projected value is the mean of six models averaged over the region.

Distribution Centre for collecting and archiving the model data. The authors are thankful to Dr. Bofu Yu who gave helpful comments and the original FORTRAN code of the program CLG2RF.

References

- Brown, L.C., Foster, G.R., 1987. Storm erosivity using idealized intensity distributions. *Trans. ASAE* 30, 379–386.
- Flanagan, D.C., Nearing, M.A. (Eds.), 1995. USDA-Water Erosion Prediction Project: Hillslope Profile and Watershed Model Documentation. NSERL Report No.10. West Lafayette, Ind., USDA-ARS Nat. Soil Erosion Research Lab.
- Giorgi, F., Mearns, L.O., 2002. Calculation of average, uncertainty range and reliability of regional climate changes from AOGCM simulations via the "Reliability Ensemble Averaging (REA)" method. *J. Clim.* 15, 1141–1158.
- Giorgi, F., Bi, X., 2005. Regional changes in surface climate interannual variability for the 21st century from ensembles of global model simulations. *Geophys. Res. Lett.* 32, L13701.
- Groisman, P.Y., Knight, R.W., Easterling, D.R., Karl, T.R., Hegerl, G.C., Razuvaev, V.N., 2005. Trends in intense precipitation in the climate record. *J. Clim.* 18, 1326–1350.
- Intergovernmental Panel on Climate Change (IPCC), 2007. *Climate Change, 2007. The physical science basis*. In: Solomon, S. et al. (Eds.), Contribution of Working Group I to the Fourth Assessment Report of the Intergovernmental Panel on Climate Change, Cambridge University Press, Cambridge, UK.
- Kharin, V.V., Zwiers, F.W., Zhang, X., Hegerl, G.C., 2007. Changes in temperature and precipitation extremes in the IPCC ensemble of global coupled model simulations. *J. Clim.* 20, 1419–1444.
- Kripalani, R.H., Oh, J.H., Chaudhari, H.S., 2007. Response of the East Asian summer monsoon to doubled atmospheric CO₂: coupled climate model simulations and projections under IPCC AR4. *Theor. Appl. Climatol.* 87, 1–28.
- Lee, E., Kwon, W., Baek, H., 2008. Summer precipitation changes in Northeast Asia from the AOGCM global warming experiments. *J. Meteorol. Soc. Jpn.* 86 (4), 475–490.
- Liu, B., Xu, M., Henderson, M., Qi, Y., Li, Y., 2004. Taking China's temperature: daily range, warming trends, and regional variations, 1955–2000. *J. Clim.* 17, 4453–4462.
- Murphy, J.M., 1999. An evaluation of statistical and dynamical techniques for downscaling local climate. *J. Clim.* 12, 2256–2284.
- Mearns, L.O., Rosenzweig, C., Goldberg, R., 1997. Mean and variance change in climate scenarios: methods, agricultural applications, and measures of uncertainty. *Clim. Change* 35, 367–396.
- National Bureau of Statistics of China (NBSC), 1998–2003. *China Statistics Yearbook*. China Statistics Press, Beijing.
- Nearing, A.M., 2001. Potential changes in rainfall erosivity in the US with climate change during the 21st century. *J. Soil Water Conserv.* 56 (3), 29–232.
- Nearing, M.A., Jetten, V., Baffaut, C., Cerdan, O., Couturier, A., Hernandez, M., Le Bissonnais, Y., Nichols, M.H., Nunes, J.P., Renschler, C.S., Souchere, V., van Oost, K., 2005. Modeling response of soil erosion and runoff to changes in precipitation and cover. *Catena* 61, 131–154.
- Nicks, A.D., Gander, G.A., 1994. CLIGEN: a weather generator for climate inputs to water resource and other models. In: *Proceedings of the 5th International Conference on Computers in Agriculture*, American Society of Agricultural Engineers, St. Joseph, Michigan, pp. 3–94.
- Nicks, A.D., Lane, L.J., Gander, G.A., 1995. Weather generator. In: Flanagan, D.C., Nearing, M.A. (Eds.), *USDA-Water Erosion Prediction Project: Hillslope Profile and Watershed Model Documentation*. NSERL Report No. 10. USDA-ARS Nat. Soil Erosion Research Lab., West Lafayette, IN (Chapter 2).
- NRC, 2003. *Understanding Climate Change Feedbacks*. Report of the Panel on Climate Change Feedbacks, National Research Council. National Academies Press, Washington, 166pp.
- Pruski, F.F., Nearing, M.A., 2002a. Runoff and soil-loss responses to changes in precipitation: a computer simulation study. *J. Soil Water Conserv.* 57 (1), 7–16.
- Pruski, F.F., Nearing, M.A., 2002b. Climate-induced changes in erosion during the 21st century for eight US locations. *Water Resour. Res.* 38 (12), 1298.
- Qian, W., Lin, X., 2005. Regional trends in recent precipitation indices in China. *Meteorol. Atmos. Phys.* 90, 193–207.
- Renard, K.G., Freidmund, J.R., 1994. Using monthly precipitation data to estimate the R-factor in the revised USLE. *J. Hydrol.* 157, 287–306.
- Renard, K.G., Foster, G.R., Weesies, G.A., McCool, D.K., Yoder, D.C., 1997. *Predicting Soil Erosion by Water: A Guide to Conservation Planning with the Revised Universal Soil Loss Equation (RUSLE)*. Agriculture Handbook No. 703. US Department of Agriculture, 404pp.
- SAS Institute Inc., 2003. *SAS/STAT® 9.1 User's Guide*. SAS Institute Inc., Cary, NC.
- Vidal, J.-P., Wade, S.D., 2008. Multimodel projections of catchment-scale precipitation regime. *J. Hydrol.* 353, 143–158.
- Wilks, D.S., 1999. Multisite downscaling of daily precipitation with a stochastic weather generator. *Climate Res.* 11, 125–136.
- Wischmeier, W.H., Smith, D.D., 1978. *Predicting Rainfall Erosion Losses: A Guide to Conservation Planning*. USDA Agricultural Handbook 537. Washington, DC, USDA.
- Wu, Y.Q., Zheng, Q.H., Zhang, Y.G., Liu, B.Y., Cheng, H., Wang, Y.Z., 2008. Development of gullies and sediment production in the black soil region of northeastern China. *Geomorphology* 101, 683–691.
- Yu, B., 2002. Using CLIGEN to generate RUSLE climate inputs. *Trans. ASAE* 45, 993–1001.
- Yu, B., 2003. An assessment of uncalibrated CLIGEN in Australia. *Agric. Forest Meteorol.* 119, 131–148.
- Zhai, P.M., Zhang, X.H., Wu, H., Pan, X., 2005. Trends in total precipitation and frequency of daily precipitation extremes over China. *J. Climate* 18, 1096–1108.
- Zhang, G.H., Nearing, M.A., Liu, B.Y., 2005. Potential effects of climate change on rainfall erosivity in the Yellow River basin of China. *Trans. ASAE* 48, 511–517.
- Zhang, X.C., 2005. Spatial downscaling of global climate model output for site-specific assessment of crop production and soil erosion. *Agric. Forest Meteorol.* 135, 215–229.
- Zhang, X.C., 2007. A comparison of explicit and implicit spatial downscaling of GCM output for soil erosion and crop production assessments. *Climate Change* 84, 337–363.
- Zhang, X.C., Nearing, M.A., Garbrecht, J.D., Steiner, J.L., 2004. Downscaling monthly forecasts to simulate impacts of climate change on soil erosion and wheat production. *Soil Sci. Soc. Am. J.* 68, 1376–1385.
- Zhang, Y.G., Wu, Y.Q., Liu, B.Y., Zheng, Q.H., Yin, J.Y., 2007. Characteristics and factors controlling the development of ephemeral gullies in cultivated catchments of black soil region, Northeast China. *Soil Till. Res.* 96, 28–41.